Research Square

Preprints are preliminary reports that have not undergone peer review.
They should not be considered conclusive, used to inform clinical practice,
or referenced by the media as validated information.

Performance Evaluation of PPP Integrity Monitoring Based on Multiple Hypothesis Solution Separation for BDS/GPS/Galileo

Yunfei Ling
National Time Service Center,Chinese Academy of Sciences
Lihong Fan
fanlihong@ntsc.ac.cn
National Time Service Center,Chinese Academy of Sciences
Xiaochun Lu
National Time Service Center,Chinese Academy of Sciences
Zhen Jiang
National Time Service Center,Chinese Academy of Sciences
Junqiang Han
National Time Service Center,Chinese Academy of Sciences
Rui Zhang
National Time Service Center,Chinese Academy of Sciences

Research Article

Keywords: Multiple Hypothesis, Solution Separation, Integrity Monitoring, Protection Level, Fault Detection and Exclusion, Performance Evaluation

Posted Date: November 18th, 2026

DOI: https://doi.org/10.21203/rs.3.rs-10662093/v1

License: This work is licensed under a Creative Commons Attribution 4.0 International License.
Read Full License

Additional Declarations: No competing interests reported.

Performance Evaluation of PPP Integrity Monitoring Based on Multiple Hypothesis Solution Separation for BDS/GPS/Galileo

Ling Yunfei [1,2], Fan Lihong [1,2,*], Lu Xiaochun [1,2], Jiang Zhen [1], Han Junqiang [1,2], Zhang Rui [1,2],

1. National Time Service Center, Chinese Academy of Sciences, 710600, Xi'an, China
2. University of Chinese Academy of Sciences, 100049, Beijing, China

*Correspondence: fanlihong@ntsc.ac.cn

E-mail address: lingyunfei@ntsc.ac.cn

Acknowledgments

This work was supported by the Youth Innovation Promotion Association CAS (Grant No.2023426), and the Research Fund of the National Natural Science Foundation of China (No.12203060). We also thank the anonymous reviewers for helping to improve the manuscript, and the International GNSS Service (IGS) and Wuhan University for providing the data and products for this study.

Abstract

Integrity monitoring is a crucial technique for ensuring the reliability of Global Navigation Satellite System (GNSS) navigation and positioning. While Precise Point Positioning (PPP) currently meets the high-precision requirements of most applications, safety-critical applications such as UAVs and autonomous driving, impose even stricter demands on the reliability of PPP. How to maintain both high precision and high integrity simultaneously remains a challenge. To achieve this goal, conducting research on integrity monitoring for PPP is of paramount importance. This study systematically evaluated the PPP integrity monitoring performance of BDS, GPS, and Galileo constellations respectively, using the Multiple Hypothesis Solution Separation (MHSS) algorithm as the core framework. This study selected observation data collected on July 1, 2025, from 18 globally distributed MGEX (Multi-GNSS Experiment) stations, along with precise ephemeris and clock products

provided by an analysis center at Wuhan University. By simulating faults, we assessed the capability of the MHSS algorithm in calculating the protection level (PL) and performing fault detection and exclusion (FDE) for BDS, GPS, and Galileo constellations. The results indicated that the average horizontal protection level (HPL) and vertical protection level (VPL) for the BDS, GPS, and Galileo constellations was 3.009 m, 2.305 m, 5.259 m and 2.143 m, 1.594 m, 3.863 m, respectively. The global average availability of integrity monitoring for BDS, GPS, and Galileo in the horizontal direction reached 82.41%, 93.07%, 68.30%, and in the vertical direction was 81.69%, 89.80%, 63.62%, respectively. Moreover, BDS demonstrated superior integrity monitoring service performance in the mid-latitude Asia-Pacific region. Under simulated step faults in pseudorange and carrier-phase observations, the average fault detection rates for BDS, GPS, and Galileo reached 89.86%, 83.71%, 92.41% and 96.02%, 94.21%, 95.66%, respectively. At fault-free epochs, the PL consistently bounded the positioning error (PE). However, due to the re-initialization of the covariance matrix during fault exclusion, the PL exhibited a re-convergence behavior.

Keywords: Multiple Hypothesis; Solution Separation; Integrity Monitoring; Protection Level; Fault Detection and Exclusion; Performance Evaluation

Introduction

Precise Point Positioning (PPP) is an absolute positioning technique that leverages pseudorange and carrier-phase observations, mitigated by precise orbits and clock products along with refined error models [1-2]. It provides high-precision positioning services, achieving decimeter-level accuracy for kinematic scenarios and centimeter-level accuracy for static scenarios [3]. While currently PPP satisfies high-precision requirements of most applications, safety-critical applications such as autonomous driving impose stricter demands on its reliability [4-5]. Anomalies in PPP services can lead to a significant positioning error (PE). Critically, if these PEs exceed the alert limit without triggering an alarm to the user, both the safety and reliability of the navigation service will be threatened [6-7]. Given that the reliability of PPP is highly dependent on the quality of observation data, any fault may propagate into a large substantial error. To meet the reliability requirements of safety-critical

applications, it is essential to conduct integrity monitoring research for PPP [8]. Although existing studies have applied integrity into PPP [9], striking a balance between high integrity and high precision still remains an urgent challenge.

Integrity monitoring refers to the capability of navigation systems to promptly alert users when faults occur or PEs exceed certain threshold [10-11]. Blanch J. et al. from the Global Positioning System (GPS) Laboratory at Stanford University drew on the multi-hypothesis solution separation integrity theory from the aviation field and adapted the integrity monitoring framework of the Advanced Receiver Autonomous Integrity Monitoring (ARAIM) algorithm for PPP [12]. Multiple Hypothesis Solution Separation (MHSS) operates multiple subset filters in parallel to achieve fault tolerance, where each filter is tolerant to a specific fault or fault set. Compared with the method based on the sum of squared residuals, solution separation has been demonstrated to provide tighter protection level and superior computational efficiency.

PPP integrity monitoring primarily comprises two components: protection level (PL) calculation and fault detection and exclusion (FDE). PL is used to monitor positioning integrity by bounding the PE, and is benchmarked against the alert limit under a predefined integrity risk probability. When both PL and PE are below the alert limit, system operation is deemed normal., otherwise, integrity monitoring is considered unavailable. Fault detection (FD) aims to detect faults through hypothesis testing [13], while fault exclusion (FE) seeks to identify and remove fault sources to mitigate unacceptable PE, thereby safeguarding the reliability and continuity of the navigation service [14]. Blanch J et al. integrated the traditionally discrete FD and FE processes by constructing confidence regions in the state space instead of relying on single-point estimates. Using GPS/Galileo constellations, the proposed method reduced the PL by nearly 50% compared to the conventional approaches, and the designed estimator performed within 20% of the theoretical lower bound [15]. To extend the method to multi-sensor fusion scenarios such as PPP, Blanch J et al. further generalized this estimator within a Kalman filter framework, validating the practical feasibility of the integrity-based estimation algorithm described in [15] using GPS/Galileo constellations [16].

Regarding fault modeling for PPP, Wang R et al. systematically analyzed recent rapid

fault events in GPS/Galileo constellations and proposed a fault model, which encompasses its definition, occurrence rate, and satellite/constellation fault probability, providing a theoretical basis for the standardization of the integrity service of PPP [17]. Lai Yu-fang et al. introduced an additional state parameter to estimate and capture satellite clock or ephemeris fault, enabling direct fault detection and identification in the pseudorange domain. Using GPS constellation, the method was verified to not only effectively handle single-satellite fault but also address the issue where clock and ephemeris fault mask each other in localized regions, successfully detecting a real-world satellite clock fault [18].

Although the aforementioned methods have been applied to integrity monitoring, existing research on the integrity monitoring of PPP primarily focuses on the calculation of PL and FDE in multi-GNSS scenarios. Due to differences in satellite geometry and redundancy among different navigation systems [19], the integrity monitoring performance of PPP based on a certain constellation remains unclear. Therefore, based on the MHSS algorithm framework, this study conducts a performance evaluation of PPP integrity monitoring for BDS, GPS, and Galileo constellations.

Methods

The principle of MHSS involves operating a bank of parallel extended Kalman filters, each designed to tolerate to a specific fault or fault set. FDE is performed by analyzing the difference between the all-in-view solution and the fault-tolerant subset solution [12]. In PPP, integrity monitoring is implemented via the MHSS algorithm by constructing the PL. As a core integrity metric, the PL is an upper bound on the PE calculated based on scenario-specific integrity risk requirements and the current user state. It establishes a confidence boundary around the positioning solution that satisfies the integrity risk, thereby reflecting the reliability of the current navigation solution. A complete proof of integrity for PL can be found in [20], and it is defined as follows:

$$\mathrm{Prob}(\mathrm{PE} > \mathrm{PL} \& \mathrm{d} < \mathrm{T}) \leq \mathrm{PHMI} \tag{1}$$

Where PE denotes the position error, d is the test statistic constructed based on the solution separation algorithm, T is the test threshold, PHMI (Probability of Hazardously Misleading Information) is the integrity risk specified by systems.

The definition of the above-mentioned PL is expanded as follows:

$$\mathrm{Prob}(|e^T(x-\hat{x})| > PL \& y \in \Omega) = \sum_{i=0}^{N} \mathrm{Prob}(|e^T(x-\hat{x})| > PL \& y \in \Omega | H_i)\, P(H_i) \quad (2)$$

Where x denotes the state vector, $\hat{x}$ is the estimated state vector derived from the all-in-view solution, y denotes the measurement vector, which represents all measurements up to time t for the Kalman filter solution, H_i refers to the $i-th$ fault hypothesis, $P(H_i)$ corresponds to the prior fault probability of the $i-th$ fault mode.

Assuming the existence of an optimal all-in-view estimator, the following key property holds for each fault-tolerant filter [20]:

$$\sigma_{ss}^{(i)2} = \sigma^{(i)2} - \sigma^{(0)2} = P^{(i)} - P^{(0)} \quad (3)$$

Where $\sigma_{ss}^{(i)}$ is the standard deviation of the solution separation under nominal conditions, $\sigma^{(i)2}$ is the variance of the estimation error of the $i-th$ subset filter (index 0 corresponds to the all-in-view filter), and $P^{(i)}$ is the covariance matrix of the fault-tolerant subset solution.

In solution separation, the detection region is defined as the difference between the fault-tolerant subset solution and the all-in-view solution:

$$\Omega_{ss} = \left\{ y \middle| \left| e^T\left(\hat{x} - \hat{x}^{(i)}\right) \right| \le T_i \right\} \quad (4)$$

Here, $\hat{x}^{(i)}$ denotes the position estimate that is fault-tolerant to the fault mode i, $e^T(\hat{x} - \hat{x}^{(i)})$ is the test statistic. The threshold T_i is to satisfy the predefined false alarm probability P_{fa} under nominal conditions:

$$T_i = Q^{-1}\left(\frac{\alpha_i}{2} P_{fa}\right) \sigma_{ss}^{(i)} \quad (5)$$

Where α_i is the false alarm probability allocated to fault mode i, and for all fault modes, the sum of their values does not exceed 1. $Q(x) = \frac{1}{\sqrt{2\pi}} \int_x^{+\infty} e^{-\frac{t^2}{2}} dt$ is the complementary cumulative distribution function of standard normal distribution, and Q^{-1} is its inverse function.

To comply with the system's predefined integrity risk, the following formula applies:

$$\mathrm{Prob}(|e^T(x-\hat{x})| > PL \& y \in \Omega) = \sum_{i=0}^{N} \mathrm{Prob}(|e^T(x-\hat{x})| > PL \& y \in \Omega | H_i)\, P(H_i) \le PHMI \quad (6)$$

Assuming that the PE and the test statistic of solution separation follow the standard Gaussian distribution, we have:

$$2Q\left(\frac{PL_i}{\sigma^{(0)}}\right)+\sum_{i=0}^{N}Q\left(\frac{PL_i-T_i}{\sigma^{(i)}}\right)P(H_i)\le PHMI \tag{7}$$

Given the calculation load of the above formula, and that PPP is mostly used for high-precision positioning related to life safety, the formula is simplified. By adopting the conventional risk equalization method, where the integrity risk is equally distributed across all fault modes, the equation reduces to:

$$\begin{cases}\sum_{i=0}^{N}Q\left(\frac{PL_i-T_i}{\sigma^{(i)}}\right)P(H_i)\le PHMI\\ PHMI=\sum_{i=0}^{N}PHMI_i\end{cases} \tag{8}$$

For the fault mode i, the following inequality is obtained:

$$Q\left(\frac{PL_i-T_i}{\sigma^{(i)}}\right)\le\frac{PHMI}{N\cdot P(H_i)} \tag{9}$$

Consequently, the definition the PL is derived. This method provides an approximate PL for solution separation, using a mathematically conservative upper bound to simplify calculations. It obviates the need for numerical searches for the worst-case deviations for each fault mode, thereby significantly reducing calculation complexity while ensuring integrity [12]:

$$PL=\max\left(T_i+Q^{-1}\left(\frac{PHMI}{N\cdot P(H_i)}\right)\sigma^{(i)}\right) \tag{10}$$

Given a specified false alarm probability P_{fa}, any allocation scheme that satisfies $\sum_i \alpha_i = 1$ is valid. For the risk equalization method, the false alarm probability budget is equally allocated among all fault modes:

$$\begin{cases}T_i=Q^{-1}(\alpha_i P_{fa})\sigma_{ss}^{i}\\ \alpha_i=\frac{1}{N}\end{cases} \tag{11}$$

Experiment description and results

This section first introduces the Experimental Setup. Then, based on the Experimental Setup, kinematic PPP was employed to derive the PEs and PLs of standalone BDS, GPS, and Galileo constellations. Subsequently, availability was analyzed based on these calculated metrics. Finally, a scheme of step fault injection was devised to scrutinize the test statistic before and after FE, as well as the fault detection rate. The following subsections provides a detailed analysis from the aspects of the PL, availability, and the FDE performance.

Experimental Setup

To analyze the availability of PPP integrity monitoring for standalone constellations, data from 18 globally distributed MGEX stations on July 1, 2025, were utilized, as shown in Figure 1.

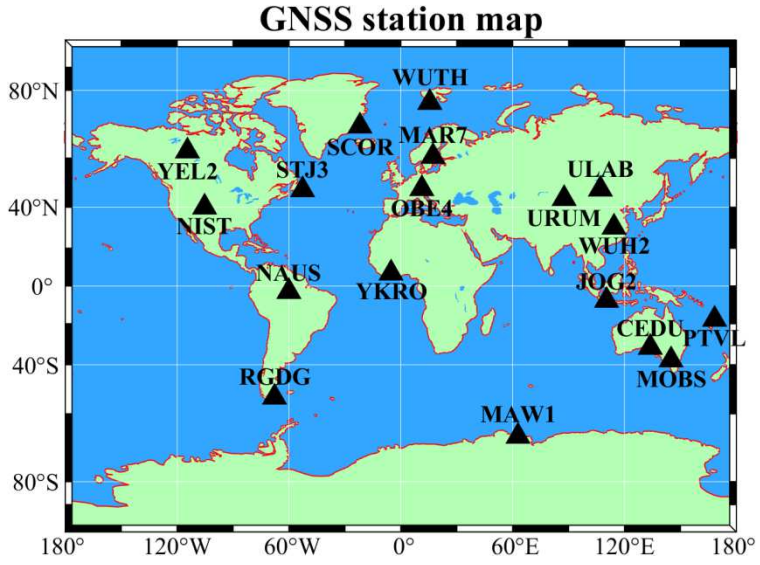


Fig. 1. Distribution of MGEX stations

This study designed three experimental scenarios for standalone BDS, GPS and Galileo constellations. Employing dual-frequency ionosphere-free combination, the availability of PPP integrity monitoring based on MHSS algorithm was evaluated. The input parameters of the integrity monitoring algorithm are listed in Table 1 [21]:

Table 1. Input parameters of the integrity monitoring algorithm

Parameter	Value
Continuity risk	1×10^{-6}
Integrity risk	1×10^{-7}
Prior fault probability of satellite	1×10^{-4}
Sampling interval	$30s$
Cutoff elevation angle	5°
Horizontal alert limit (HAL)	2.5m
Vertical alert limit (VAL)	2m

Protection Level

To analyze the availability of the standalone BDS, GPS, and Galileo constellations, the average PEs and PLs at each station for each constellation were calculated, as shown in Fig. 2 and Fig. 3, respectively. The constellation-wide averages across all stations for BDS, GPS, and Galileo were also statistically summarized, as listed in Table 2.

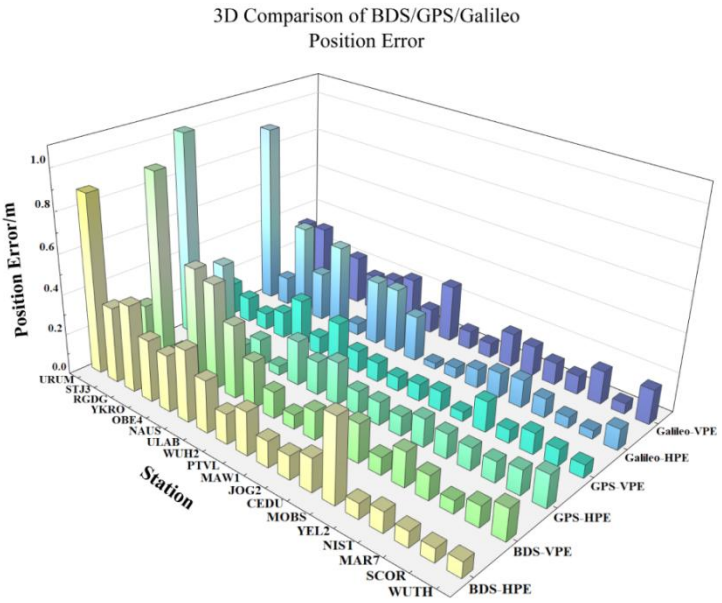


Fig. 2. Average positioning error of BDS/GPS/Galileo

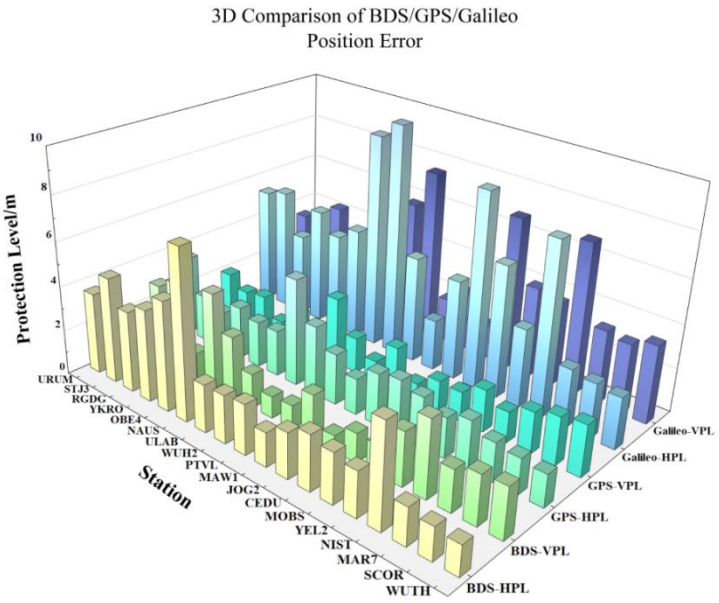


Fig. 3. Average protection level of BDS/GPS/Galileo

Table 2. Average positioning error and protection level of BDS/GPS/Galileo across all stations

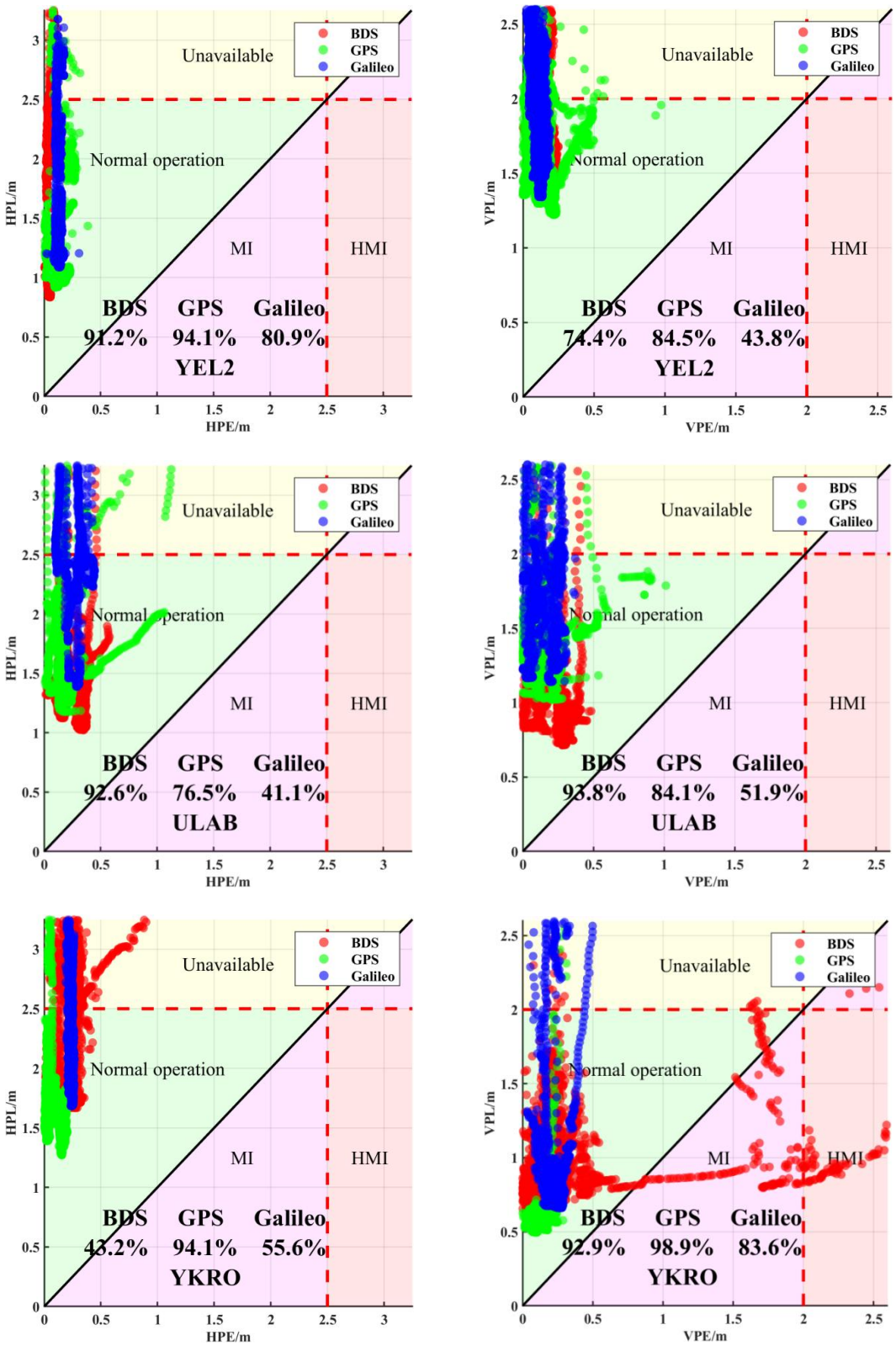
GNSS	HPE-RMS(m)	VPE-RMS(m)	HPL-RMS(m)	VPL-RMS(m)
BDS	0.247	0.234	3.009	2.143
GPS	0.193	0.112	2.305	1.594
Galileo	0.215	0.171	5.259	3.863

In Figs. 2 and 3, BDS-HPE refers to the average horizontal PE using standalone BDS constellation, and BDS-HPL refers to the average horizontal protection level using the same constellation. The same naming convention applies analogously to the other constellations. With the combination of Figs. 2, 3 and Table 2, the average positioning accuracy of BDS, GPS, Galileo across all stations reached the decimeter level, and the average PL reached the meter level. Specifically, GPS yielded a smaller PE among the three; whereas BDS provided a tighter PL than Galileo. This performance discrepancy was attributed to Galileo's comparatively sparse satellite visibility, which degraded the geometry distribution of Galileo and consequently necessitated a more conservative PL.

Analysis of Availability

Based on the derived PEs and PLs, the availability of the integrity monitoring of the

standalone BDS, GPS, and Galileo constellations across the 18 stations was statistically evaluated separately. The performance of the integrity monitoring method was assessed using the Stanford diagram. For illustrative purposes, one representative station from each of the high-, mid-, and low-latitude regions (YEL2, ULAB, and YKRO) was selected for demonstration, as shown in Fig. 4.



222 Fig. 4. Stanford diagram for integrity monitoring of different constellations; red dots denote
223 BDS, green dots denote GPS, and blue dots denote Galileo, (a) Stanford diagram for integrity
224 monitoring at station ULAB (Up); (b) Stanford diagram for integrity monitoring at station
225 ULAB (Mid); (c) Stanford diagram for integrity monitoring at station YKRO (Low)

Fig. 4 shows the integrity availability across the three representative stations. At station YEL2, the horizontal and vertical availability of BDS, GPS, Galileo were 91.2%, 94.1%, 80.9% and 74.4%, 84.5%, 43.8%, respectively. At station ULAB, the horizontal and vertical availability were 92.6%, 76.5%, 41.1% and 93.8%, 84.1%, 51.9%, respectively. At station YKRO, the horizontal and vertical availability were 43.2%, 94.1%, 55.6% and 92.9%, 98.9%, 83.6%, respectively. Due to fewer visible satellites and reduced redundancy, the availability of Galileo was degraded in high-latitude regions.

To facilitate a more intuitive cross-station comparison, Tables 3 and 4 listed the availability of the integrity monitoring of the BDS, GPS, and Galileo constellations in the horizontal and vertical directions across all the selected 18 stations, respectively.

238 Table 3. Availability of the integrity monitoring of BDS, GPS, and Galileo in the horizontal
239 direction at each station

GNSS	BDS		GPS		Galileo	
Station	PMI	Available	PMI	Available	PMI	Available
SCOR	0.0%	96.1%	0.0%	94.5%	0.0%	91.3%
YKRO	0.0%	43.2%	0.0%	94.1%	0.0%	55.6%
RGDG	0.0%	81.7%	0.0%	96.7%	0.0%	80.9%
JOG2	0.0%	95.1%	0.0%	95.5%	0.0%	71.1%
CEDU	0.0%	92.0%	0.0%	94.1%	0.0%	69.7%
MOBS	0.0%	94.3%	0.0%	94.7%	0.0%	75.1%
PTVL	0.0%	94.0%	0.0%	94.5%	0.0%	53.6%
MAW1	0.0%	96.8%	0.0%	95.2%	0.0%	92.3%
YEL2	0.0%	91.2%	0.0%	94.1%	0.0%	80.9%
NIST	0.0%	71.9%	0.0%	96.7%	0.0%	51.2%
STJ3	0.0%	76.7%	0.0%	94.1%	0.0%	50.0%
NAUS	0.0%	34.9%	0.0%	95.3%	0.0%	51.3%
MAR7	0.0%	96.4%	0.0%	95.8%	0.0%	92.4%
OBE4	0.0%	46.5%	0..0%	94.9%	0.0%	75.2%
WUH2	0.0%	94.2%	0.0%	85.1%	0.0%	34.8%
ULAB	0.0%	92.6%	0.0%	76.5%	0.0%	41.1%
URUM	0.0%	88.5%	6.3%	87.3%	0.0%	70.5%
WUTH	0.0%	97.3%	0.0%	96.2%	0.0%	92.5%

240

241 Table 4. Availability of the integrity monitoring of BDS, GPS, and Galileo in the vertical
242 direction at each station

GNSS	BDS		GPS		Galileo	
Station	PMI	Available	PMI	Available	PMI	Available
SCOR	0.0%	69.6%	0.0%	72.7%	0%	29.0%
YKRO	4.2%	92.9%	0.0%	98.9%	0.0%	83.6%
RGDG	0.0%	60.1%	0.0%	95.5%	0.0%	52.2%
JOG2	0.1%	98.5%	0.0%	98.4%	0.0%	91.7%
CEDU	0.0%	95.3%	0.0%	96.9%	0.0%	80.3%
MOBS	0.0%	97.4%	0.0%	98.1%	0.0%	80.6%
PTVL	0.0%	98.1%	0.0%	98.6%	0.0%	84.1%
MAW1	0.0%	84.0%	0.0%	80.6%	0.0%	58.0%
YEL2	0.0%	74.4%	0.0%	84.5%	0.0%	43.8%
NIST	0.0%	76.1%	0.0%	95.1%	0.0%	57.4%
STJ3	0.0%	69.5%	0.0%	96.8%	0.0%	51.8%
NAUS	0.3%	80.1%	0.0%	98.9%	0.0%	90.9%
MAR7	0.0%	94.1%	0.0%	90.7%	0.0%	67.0%
OBE4	0.0%	43.8%	0.0%	96.9%	0.0%	70.8%
WUH2	0.0%	98.6%	0.0%	90.3%	0.0%	60.2%
ULAB	0.0%	93.8%	0.0%	84.1%	0.0%	51.9%
URUM	0.0%	92.5%	0.0%	93.0%	0.0%	73.4%
WUTH	0.0%	51.7%	0.0%	46.5%	0.0%	18.6%

243

244 As seen from Tables 3 and 4, misleading information was absent across the majority of
245 the selected MGEX stations, confirming that the MHSS algorithm satisfied the predefined
246 requirement of integrity risk. In addition, horizontal availability consistently surpassed
247 vertical availability at most stations, which is related to the operational configuration that the
248 horizontal alert limit (HAL) is set larger than the vertical alert limit (VAL).

249 Table 5 shows the average availability of the integrity monitoring of BDS, GPS, and
250 Galileo in low-, medium-, and high-latitude regions. Both in the horizontal and vertical
251 directions, BDS had higher availability in the mid-latitude Asia-Pacific region, which verified
252 that BDS can provide better service performances in the mid-latitude Asia-Pacific region [22].
253 Galileo maintained low average availability, a shortfall directly attributable to its sparser

constellation and inherently weaker observation geometry.

Table 5. Average availability of the integrity monitoring of BDS/GPS/Galileo in low, medium, and high latitude regions

Region/GNSS		Horizontal Direction			Vertical Direction		
		BDS	GPS	Galileo	BDS	GPS	Galileo
Low-latitude		75.58%	94.70%	62.73%	93.71%	98.30%	85.20%
Mid-latitude	Asia-Pacific	91.76%	82.96%	48.80%	94.96%	89.13%	61.83%
	Non-Asia-Pacific	78.21%	95.45%	73.50%	68.86%	91.28%	46.01%
High-latitude		95.10%	95.16%	88.56%	70.03%	70.53%	40.13%

Fault Detection and Exclusion

To evaluate the capability of the FD function of the integrity monitoring algorithm using the BDS, GPS, and Galileo constellations, a scheme of step fault injection is designed as shown in Table 6.

Table 6. The scheme of step fault injection

Injected satellite/Fault magnitude	C35	G03	E07
Pseudorange observation	10m	10m	10m
	20m	20m	20m
	30m	30m	30m
Carrier phase observation	1.5m	1.5m	1.5m
	2.0m	2.0m	2.0m
	2.5m	2.5m	2.5m

At station YEL2, step faults were injected into satellites C35, G03, and E07, respectively, with pseudorange faults of 10 m, 20 m, and 30 m and carrier phase faults of 1.5 m, 2.0 m, and 2.5 m, respectively. All injected step faults started at 15 minutes and lasted for 45 minutes until 60 minutes. On this basis, the solution separation test statistics (SS) and fault detection rate for the PPP integrity monitoring under different constellations were analyzed.

Following the scheme shown in Table 6, the maximum test statistics before fault detection and the maximum and minimum test statistics after FD were calculated for each constellation. The test statistics of solution separation for different constellations are shown in Figs. 5-10.

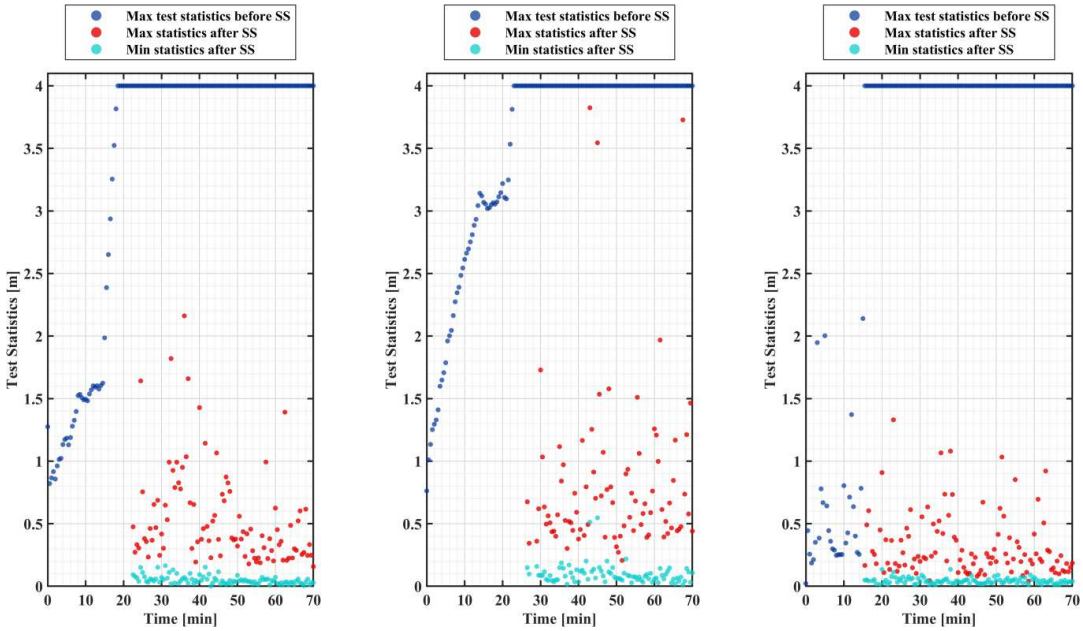


Fig. 5. SS test statistics after injecting 10m step fault into pseudorange observations of different satellites, (a) Injecting a fault into satellite C35 (Left); (b) Injecting a fault into satellite G03 (Mid); (c) Injecting a fault into satellite E07 (Right)

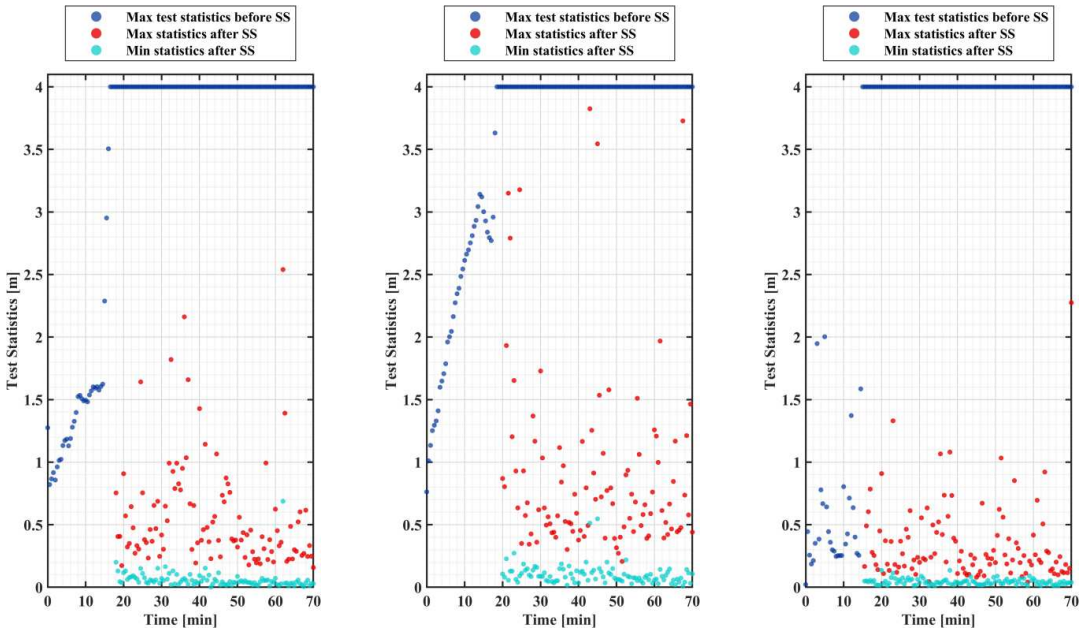
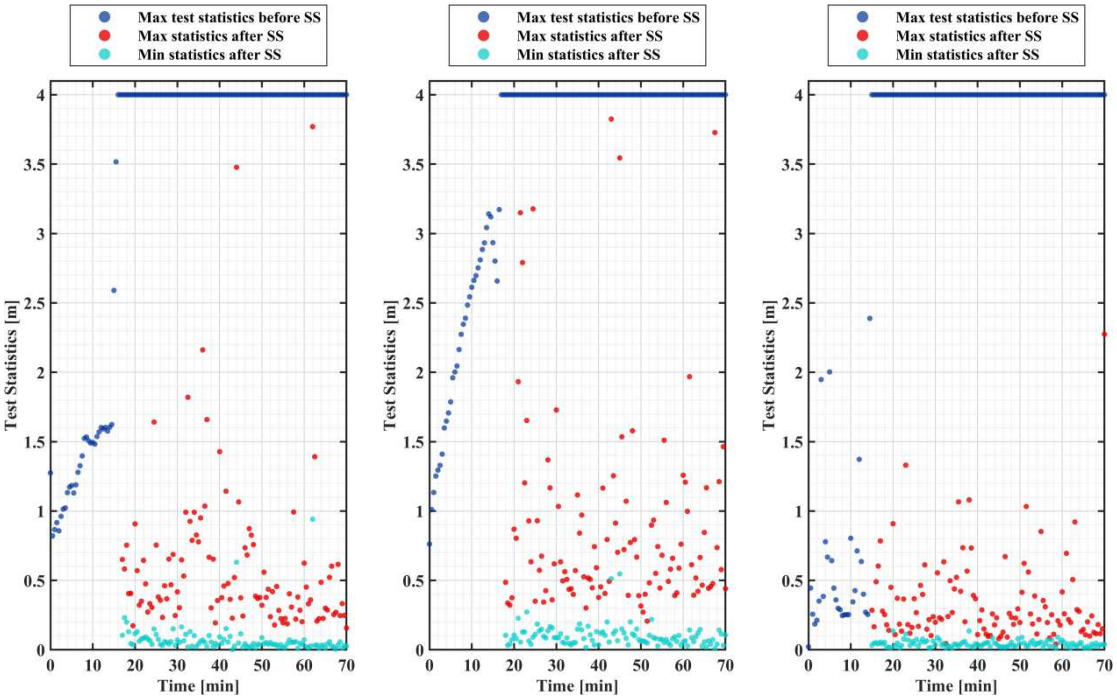
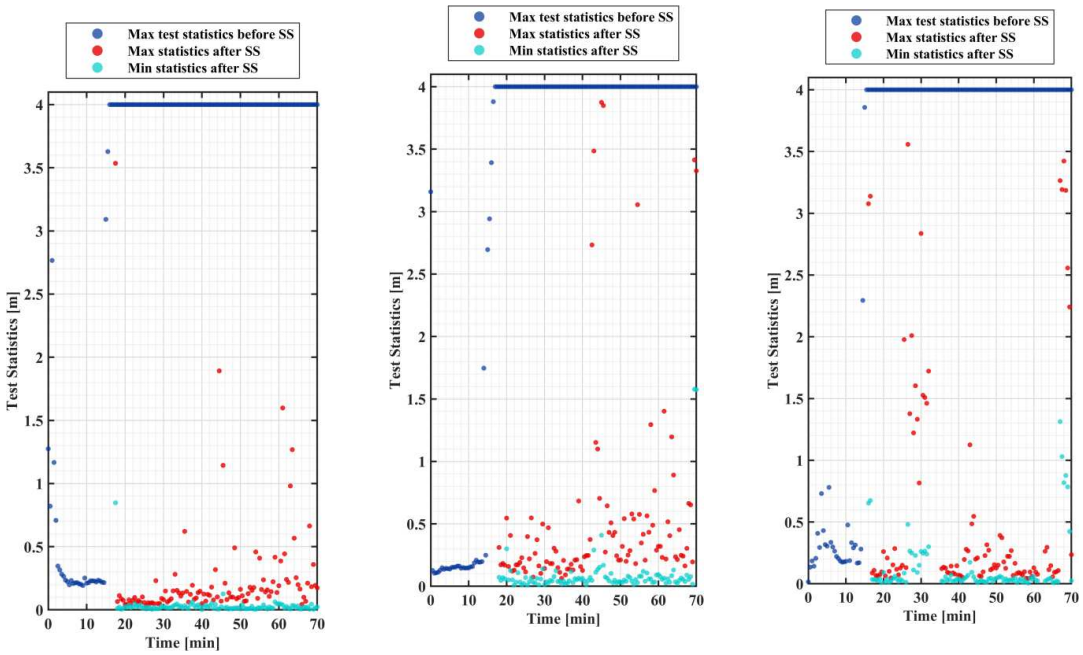


Fig. 6. SS test statistics after injecting 20m step fault into pseudorange observations of different satellites, (a) Injecting a fault into satellite C35 (Left); (b) Injecting a fault into satellite G03 (Mid); (c) Injecting a fault into satellite E07 (Right)



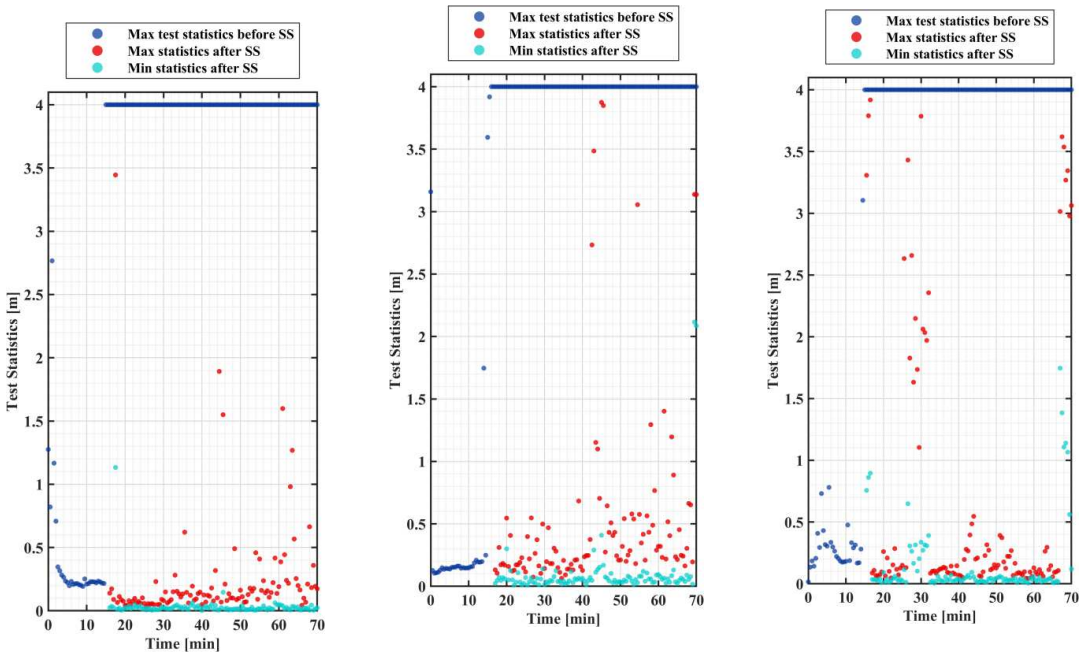
284 Fig. 7. SS test statistics after injecting 30m step fault into pseudorange observations of
285 different satellites, (a) Injecting a fault into satellite C35 (Left); (b) Injecting a fault into
286 satellite G03 (Mid); (c) Injecting a fault into satellite E07 (Right)

287

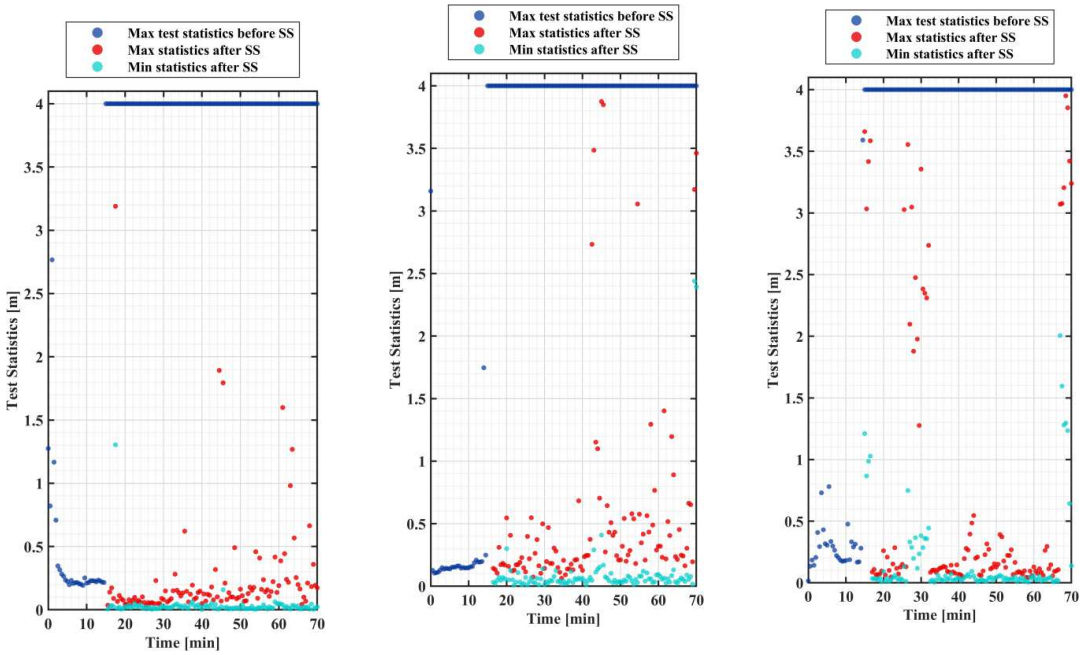


288 Fig. 8. SS test statistics after injecting 1.5m step fault into carrier phase observations of
289 different satellites, (a) Injecting a fault into satellite C35 (Left); (b) Injecting a fault into
290 satellite G03 (Mid); (c) Injecting a fault into satellite E07 (Right)

291



292 Fig. 9. SS test statistics after injecting 2.0m step fault into carrier phase observations of
293 different satellites, (a) Injecting a fault into satellite C35 (Left); (b) Injecting a fault into
294 satellite G03 (Mid); (c) Injecting a fault into satellite E07 (Right)
295



296 Fig. 10. SS test statistics after injecting 2.5m step fault into carrier phase observations of
297 different satellites, (a) Injecting a fault into satellite C35 (Left); (b) Injecting a fault into
298 satellite G03 (Mid); (c) Injecting a fault into satellite E07 (Right)
299

For clarity of presentation, test statistics exceeding 4m are truncated in the plots. As shown in Figures 5-10, when no satellite fault occurs, the test statistics remains below the threshold, rendering the solution separation-based FE mechanism dormant. As the fault injection progresses, the test statistics escalate progressively until it surpassed the threshold, thereby activating the FD and FE function. After the faulty satellite is excluded, the peak SS test statistic remains below the threshold, confirming effective fault mitigation.

It should be noted that among the three subfigures (a), (b), and (c) in Figs. 5 – 10, when the fault is initially injected, the maximum test statistic does not immediately exceed the threshold. Instead, as the fault injection continues, the maximum test statistic gradually increases until it exceeds the threshold, thereby triggering the FE function. This latency contributes to a reduced fault detection rate. The underlying cause is attributable to the filter's stabilized state, where the precomputed error covariance matrix and the gain of filter become excessively small, leading to an over-reliance on historical observation data and a sluggishly response to new observation data. Consequently, the filter reacts significantly slowly to step faults, degrading the overall performances. In addition, Figs. 5 – 10 also show the test statistics during the 10- minute interval following fault injection. It can be seen that the fault's impact persists beyond its duration, requiring a longer recovery period. Therefore, restarting the filter upon fault detection is recommended to shorten the fault duration [18].

To further compare the fault sensitivity of the BDS, GPS, and Galileo constellations, Table 7 and 8 summarize the detection rates of BDS, GPS, and Galileo under step faults of different magnitudes injected into pseudorange and carrier phase observations.

Table 7. Detection rate of different constellations under a step fault injected into pseudorange observation

Fault Magnitude /GNSS	BDS	GPS	Galileo
10m	82.61%	70.66%	95.66%
20m	92.40%	88.05%	97.83%
30m	94.57%	92.40%	98.92%
Average	89.86%	83.71%	92.41%

Table 8. Detection rate of different constellations under a step fault injected into carrier phase observation

Fault Magnitude /GNSS	BDS	GPS	Galileo
1.5m	93.48%	92.40%	90.22%
2.0m	96.74%	94.57%	97.83%
2.5m	97.83%	95.66%	98.92%
Average	96.02%	94.21%	95.66%

Tables 7 and 8 show that the fault detection rate of the constellations fails to attain 100%, irrespective of whether faults are injected into pseudorange observation or carrier phase observation, and regardless of the fault magnitude. This shortfall arises because the effect of the fault is gradually assimilated into the state estimation, resulting in a slow and progressive change in the residuals. Nevertheless, as shown in Figs. 5 – 10, as the fault continues to be injected until the test statistic first exceeds the threshold, the fault detection rate of the BDS, GPS, and Galileo constellations reaches 100%. Furthermore, compared to pseudorange faults, all constellations exhibit higher sensitivity and superior fault detection rates when faults are injected into carrier-phase observations.

Table 9 presents the average values of the test statistics of BDS, GPS, and Galileo before and after implementing solution separation for the FDE. The magnitude of the test statistic of solution separation reflects the deviation between the all-in-view solution and the subset solutions. Consequently, a smaller SS test statistic indicates higher reliability of the positioning result. In other words, a compressed test statistic implies improved reliability of the PPP float solution. Table 9 indicates that solution separation can effectively detect and remove abnormal observation data, demonstrating strong robustness.

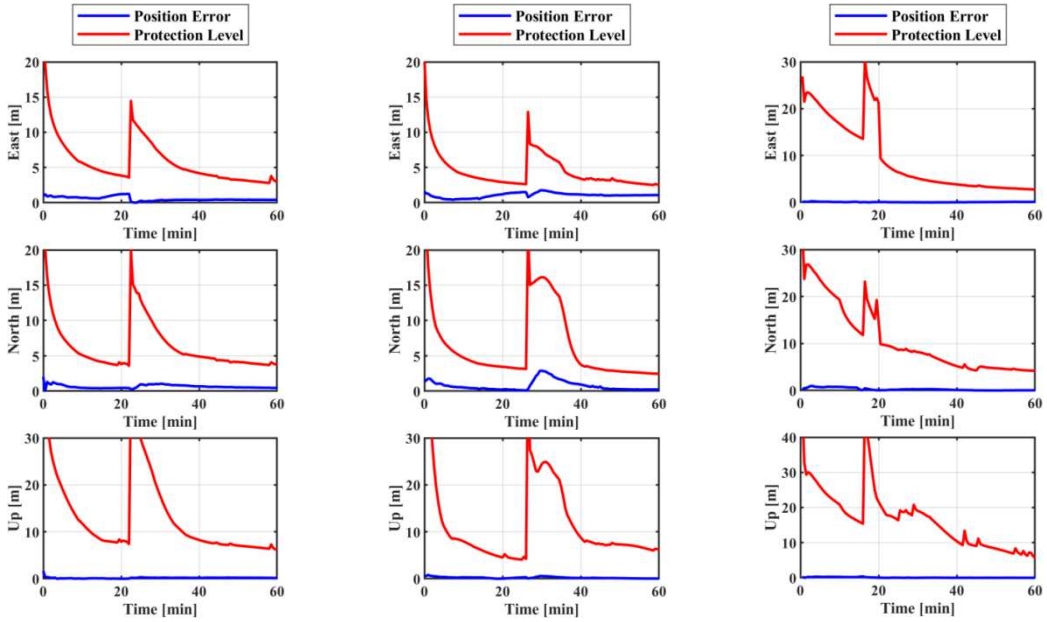
345 Table 9. Average values of the test statistics of BDS/GPS/Galileo before and after using SS

	BDS	GPS	Galileo
Average value of the test statistic before SS (m)	10.344	17.823	17.119
Average value of the test statistic after SS (m)	0.407	0.830	0.307

346

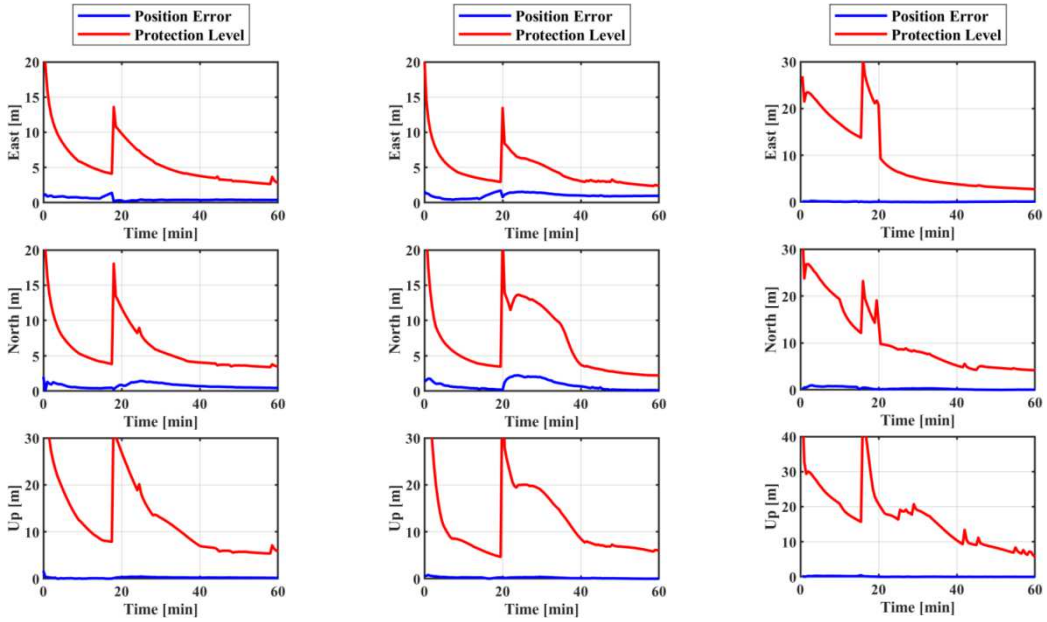
347 Figures 11 – 16 illustrate the bounding of the PEs by the PLs for BDS, GPS, and Galileo
348 following the injection of step faults of different magnitudes into pseudorange and
349 carrier-phase observations. To mitigate the sustained impact of step fault on the filter, a reset
350 mechanism is triggered upon FD. During epochs where a fault exists but is not yet detected,
351 the PE gradually accumulates. When the PE surpasses the test threshold, the FE function is
352 triggered. The identified faulty satellite is removed from all subsets, and its corresponding
353 subset solution becomes the new all-in-view solution. Throughout this process, the PL
354 consistently bounds the PE. However, due to the reinitialization of the covariance matrix and
355 the subsequent reset of all filters post-exclusion, the PL undergoes a re-convergence period.
356 Furthermore, due to the limited satellite availability and inferior geometric distribution of
357 Galileo, the PL exhibits slight fluctuations.

358



359 Fig. 11. Bounding of the positioning error by the protection level for a 10 m step fault injected
360 into pseudorange observations of different satellites, (a) Injecting a fault into satellite C35
361 (Left); (b) Injecting a fault into satellite G03 (Mid); (c) Injecting a fault into satellite E07
362 (Right)

363



364 Fig. 12. Bounding of the positioning error by the protection level for a 20 m step fault injected
365 into pseudorange observations of different satellites, (a) Injecting a fault into satellite C35
366 (Left); (b) Injecting a fault into satellite G03 (Mid); (c) Injecting a fault into satellite E07
367 (Right)

368

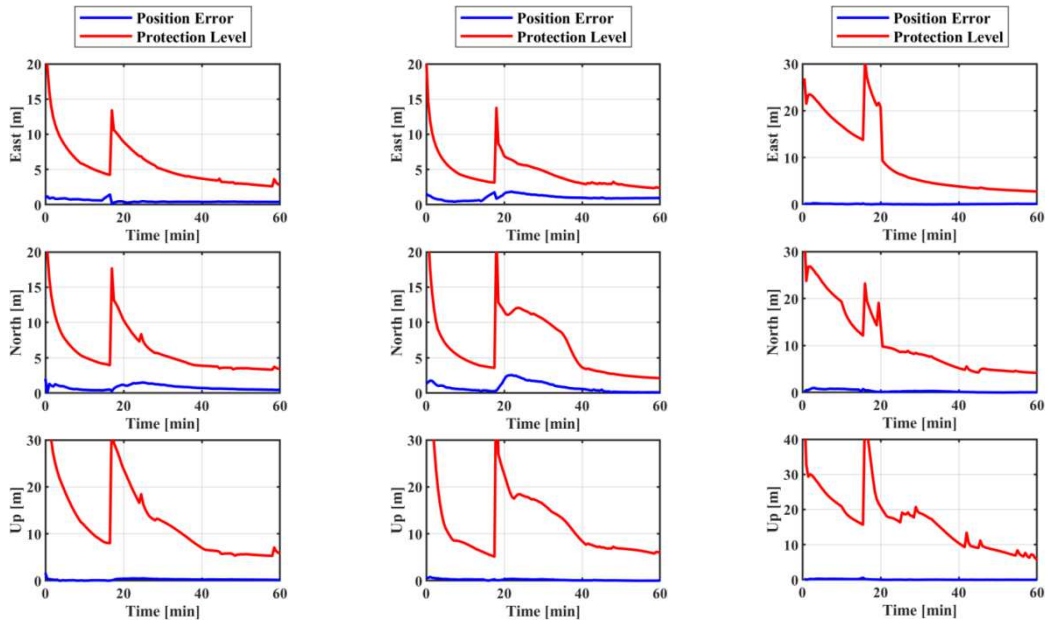


Fig. 13. Bounding of the positioning error by the protection level for a 30 m step fault injected into pseudorange observations of different satellites, (a) Injecting a fault into satellite C35 (Left); (b) Injecting a fault into satellite G03 (Mid); (c) Injecting a fault into satellite E07 (Right)

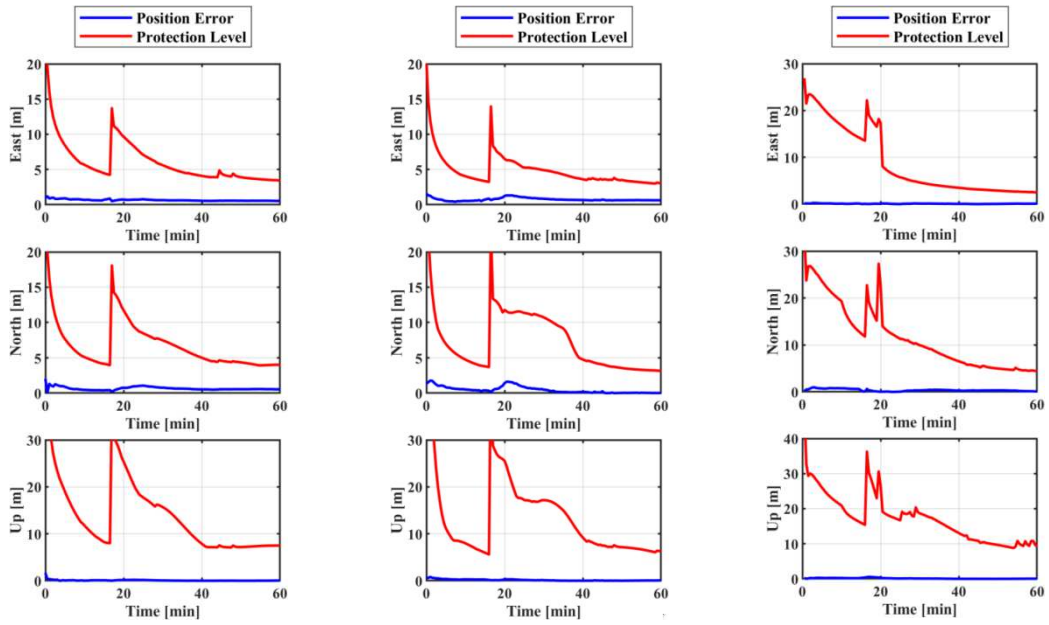
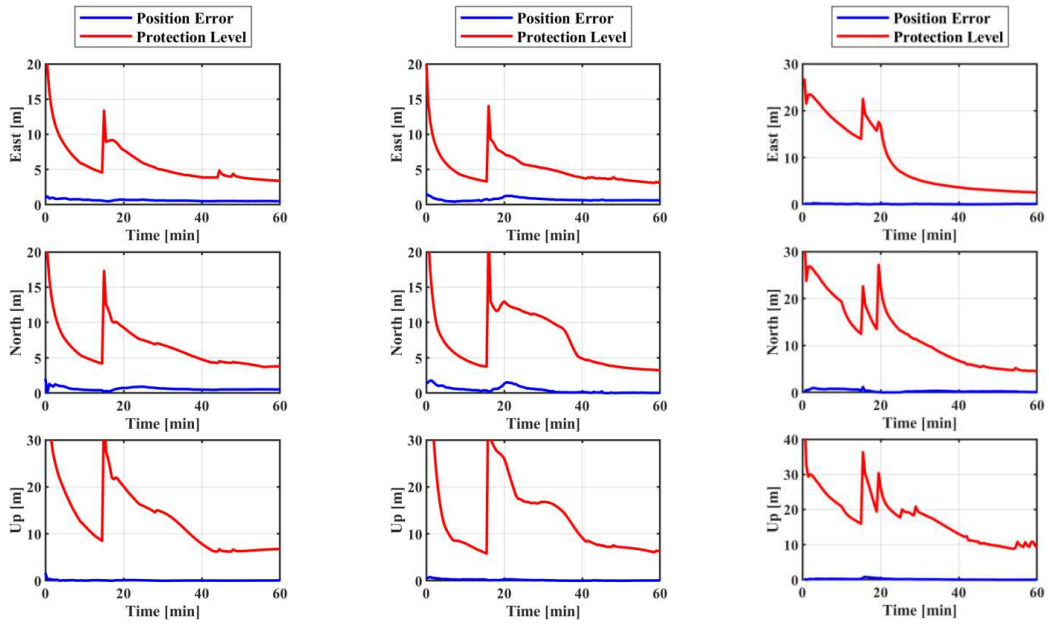
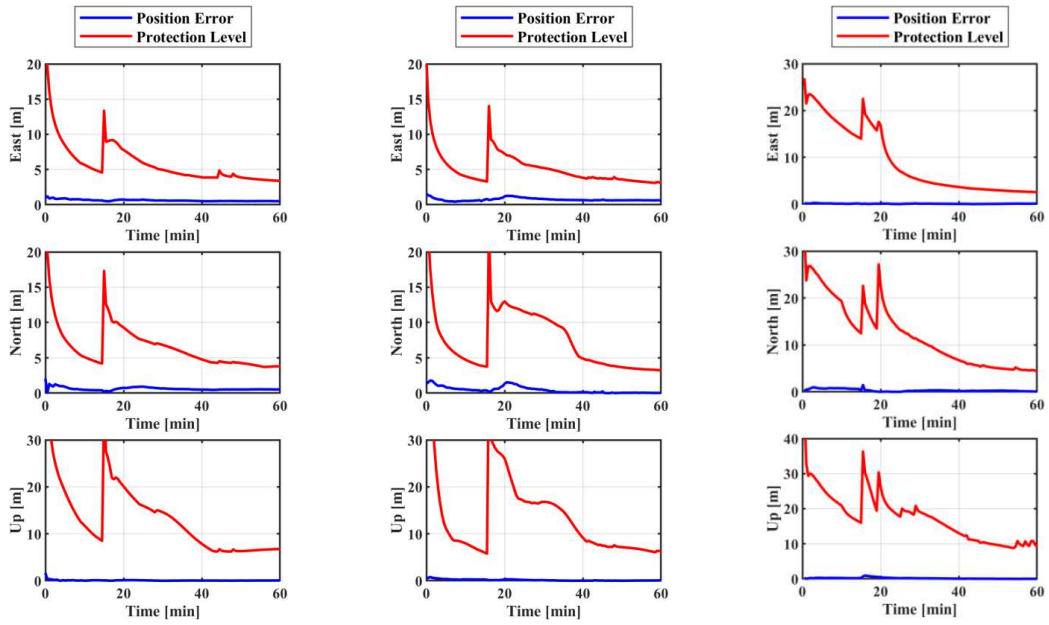


Fig. 14. Bounding of the positioning error by the protection level for a 1.5 m step fault injected into carrier phase observations of different satellites, (a) Injecting a fault into satellite C35 (Left); (b) Injecting a fault into satellite G03 (Mid); (c) Injecting a fault into satellite E07 (Right)



379 Fig. 15. Bounding of the positioning error by the protection level for a 2.0 m step fault
380 injected into carrier phase observations of different satellites, (a) Injecting a fault into satellite
381 C35 (Left); (b) Injecting a fault into satellite G03 (Mid); (c) Injecting a fault into satellite E07
382 (Right)
383



384 Fig. 16. Bounding of the positioning error by the protection level for a 2.5 m step fault
385 injected into carrier phase observations of different satellites, (a) Injecting a fault into satellite
386 C35 (Left); (b) Injecting a fault into satellite G03 (Mid); (c) Injecting a fault into satellite E07
387 (Right)
388

Conclusion

Based on observation data from 18 MGEX stations at different geographic locations around the world, as well as precise orbits and clock corrections provided by Wuhan University, this study evaluated the performance of PPP integrity monitoring for standalone BDS, GPS and Galileo constellations using the MHSS algorithm. The preliminary conclusions are as follows:

1. The average horizontal and vertical PLs for BDS, GPS, and Galileo are 3.009m, 2.305m, 5.259m and 2.143m, 1.594m, 3.863m, respectively. BDS yields a tighter PL than Galileo. This performance gap is attributed to the sparse visibility and inferior geometric distribution of Galileo, which necessitate a more conservative PL to maintain integrity assurance.

2. The global average horizontal and vertical integrity availabilities for BDS, GPS, and Galileo are 82.41%, 93.07%, 68.30% and 81.69%, 89.80%, 63.62%, respectively. Notably, BDS demonstrates superior availability performance, confirming its enhanced service capability in the mid-latitude Asia-Pacific region.

3. Under step fault injections into pseudorange and carrier-phase observations, the average fault detection rates for BDS, GPS, and Galileo are 89.86%, 83.71%, 92.41% and 96.02%, 94.21%, 95.66%, respectively. While the MHSS framework effectively mitigates faults, the detection rate falls short of 100% in prolonged scenarios due to the gradual assimilation of fault effects into the state estimation. However, the instantaneous detection rate reaches 100% once the test statistic first exceeds the threshold. Furthermore, all constellations exhibit higher sensitivity to carrier-phase faults than to pseudorange faults.

4. Following fault exclusion, the average test statistics for BDS, GPS, and Galileo are reduced to 0.407 m, 0.830 m, and 0.307 m, respectively, confirming the robustness of the solution separation approach. The PL consistently bounds the PE throughout the monitoring process. However, the reinitialization of convariance matrix during fault exclusion induces a transient re-convergence period in the PL.

Funding: This work was supported by the Youth Innovation Promotion Association CAS (Grant No.2023426), and the Research Fund of the National Natural Science Foundation of

China (No.12203060).

Conflicts of Interest: The authors declare that they have no conflict of interest.

References

[1] Zumberge J F, Heflin M B, Jefferson D C, et al. Precise point positioning for the efficient and robust analysis of GPS data from large networks[J]. Journal of Geophysical Research: Solid Earth, 1997, 102(B3): 5005-5017.

[2] Kouba J, Hérous P. Precise Point Positioning Using IGS Orbit and Clock Products[J]. GPS Solutions, 2001, 5(2): 12-28.

[3] Yang F, Zhao L, Li L, et al. Performance Evaluation of Kinematic BDS/GNSS Real-Time Precise Point Positioning for Maritime Positioning[J]. Journal of Navigation, 2019, 72(1): 34-52.

[4] Zhang Xiaohong, Li Xingxing, Guo Fei, et al. Server-based real-time precise point positioning and its application[J]. Chinese Journal of Geophysics, 2010, 53(6): 1308-1314.

[5] Ulrich W, Markus B, Chen X, et al. Integrity of the Trimble® CenterPoint® RTX Correction Service[J]. 31st International Technical Meeting of the Satellite Division of the Institute of Navigation (ION GNSS+ 2018), Miami, Florida, September 24-28, 2018.

[6] El-Mowafy A. On detection of observation faults in the observation and position domains for positioning of intelligent transport systems[J]. Journal of Geodesy, 2019, 93(10): 2109-2122.

[7] El-Mowafy A, Deo M, Kubo N. Maintaining real-time precise point positioning during outages of orbit and clock corrections[J]. GPS Solutions, 2017, 21(3): 937-947.

[8] Zhang Jie, Zhao Lin, Yang Fuxin, Sun Zhiguo, Li Liang. PPP integrity monitoring algorithm for general-purpose navigation applications[J]. Acta Aeronautica et Astronautica Sinica, 2023, 44(13): 191-201.

[9] Madrid, P. F. Navarro, Fernández, L. Martínez, López, M A, et al. PPP Integrity for Advanced Applications, Including Field Trials with Galileo, Geodetic and Low-Cost Receivers, and a Preliminary Safety Analysis[C]//29th International Technical Meeting of The Satellite Division of the Institute of Navigation (ION GNSS+ 2016). Portland,

Oregon, 2016: 3332-3354.

[10] Du Y, Wang J, Rizos C, et al. Vulnerabilities and integrity of precise point positioning for intelligent transport systems: overview and analysis[J]. Satellite Navigation, 2021, 2(1): 3.

[11] Li L, Wang H, Jia C, et al. Integrity and continuity allocation for the RAIM with multiple constellations[J]. GPS Solutions, 2017, 21(4): 1503-1513.

[12] Gunning K, Blanch J, Walter T, et al. Design and Evaluation of Integrity Algorithms for PPP in Kinematic Applications[C]//31st International Technical Meeting of The Satellite Division of the Institute of Navigation (ION GNSS+ 2018). Miami, Florida, 2018: 1910-1939.

[13] Joerger, Mathieu, Pervan, et al. Fault Detection and Exclusion Using Solution Separation and Chi-Squared ARAIM[J]. IEEE Transactions on Aerospace and Electronic Systems, 2016, 52(2): 726-742.

[14] Li L, Wang H, Jia C, et al. A proposed fault detection and exclusion method applied to multi-GNSS single-frequency[J]. GPS Solutions, 2017, 21: 1503–1513.

[15] Blanch J, Walter T. A Fault Detection and Exclusion Estimator Designed for Integrity[C]//34th International Technical Meeting of the Satellite Division of The Institute of Navigation (ION GNSS+ 2021). St. Louis, Missouri, 2021: 1672-1686.

[16] Blanch J, Lai Y F, Walter T. Integrity-Based Estimators for Precise Point Positioning and Other Applications[C]//ION 2024 Pacific PNT Meeting. Honolulu, Hawaii, 2024: 477-490.

[17] Wang R, Blanch J, Walter T. Constellation Fault Monitoring to Support a Precise Point Positioning (PPP) Integrity Service[C]//37th International Technical Meeting of the Satellite Division of The Institute of Navigation (ION GNSS+ 2024). Baltimore, Maryland, 2024: 628-642.

[18] Lai Y F, Blanch J, Walter T, et al. Prototyping Integrity Monitors for PPP Fault Detections[C]//36th International Technical Meeting of the Satellite Division of The Institute of Navigation (ION GNSS+ 2023). Denver, Colorado, 2023: 2592-2605.

[19] ZHAO Ang，YANG Yuanxi，XU Yangyin,et al. Integrity Analysis of GNSS Single System and Multi-system Combination[J]. Geomatics and Information Science of Wuhan

University，2020, 45(1): 72-80.

[20] Blanch J, Walter T, Enge P, et al. Baseline advanced RAIM user algorithm and possible improvements[J]. IEEE Transactions on Aerospace and Electronic Systems, 2015, 51(1): 713-732.

[21] Zhang J, Zhao L, Yang F, et al. Integrity monitoring for undifferenced and uncombined PPP under local environmental conditions[J]. Measurement Science and Technology, 2022, 33(6): 065010.

[22] Li Yi, Wang Li, Shu Bao, Tian Yunqing, Wang Bingjie, Peng Xin. An Optimal Allocation Method for ARAIM Risk Considering DOP[J]. Geomatics and Information Science of Wuhan University, 2025, 50(10): 2001-2012.